ADVANCED MATERIALS
www.advmat.de

Machine Learning-Enabled Tomographic Imaging of Chemical Short-Range Atomic Ordering

Yue Li, Timoteo Colnaghi, Yilun Gong,* Huaide Zhang, Yuan Yu, Ye Wei, Bin Gan, Min Song, Andreas Marek, Markus Rampp, Siyuan Zhang, Zongrui Pei, Matthias Wuttig, Sheuly Ghosh, Fritz Körmann, Jörg Neugebauer, Zhangwei Wang,* and Baptiste Gault**

In solids, chemical short-range order (CSRO) refers to the self-organization of atoms of certain species occupying specific crystal sites. CSRO is increasingly being envisaged as a lever to tailor the mechanical and functional properties of materials. Yet quantitative relationships between properties and the morphology, number density, and atomic configurations of CSRO domains remain elusive. Herein, it is showcased how machine learning-enhanced atom probe tomography (APT) can mine the near-atomically resolved APT data and jointly exploit the technique's high elemental sensitivity to provide a 3D quantitative analysis of CSRO in a CoCrNi medium-entropy alloy. Multiple CSRO configurations are revealed, with their formation supported by state-of-the-art Monte-Carlo simulations. Quantitative analysis of these CSROs allows establishing relationships between processing parameters and physical properties. The unambiguous characterization of CSRO will help refine strategies for designing advanced materials by manipulating atomic-scale architectures.

1. Introduction

Over time, strategies were developed to tailor the properties of materials to societal needs, by manipulating their compositions, structures, and imperfections from the macro- to microscale and even atomic scale. Alloy making traditionally involves the introduction of small quantities of one or more species, solutes, into a matrix of a solvent element. During processing, one or more (meta)stable phases form that modify the response to physical or mechanical stimulation.[1] In the past decade, so-called high/medium-entropy alloys (H/MEAs) have been introduced, whereby multiple elements are mixed in equal, or close to equal quantity. Although initially assumed to be chemically disordered,[2] i.e., atoms from these principal elements randomly occupy sites of the crystalline lattice, recent studies have suggested that atomic-scale, chemical short-range order (CSRO) is far more prevalent in H/MEAs than initially assumed, offering a potential lever to tailor their properties.[2b,3]

A representative H/MEA is CoCrNi, in which the presence and nature of CSRO are currently debated.[2b,3b,d–g,4] Transmission

Y. Li, Y. Gong, S. Zhang, S. Ghosh, F. Körmann, J. Neugebauer, B. Gault
Max-Planck-Institut für Eisenforschung GmbH
Max-Planck-Straße 1, 40237 Düsseldorf, Germany
E-mail: yue.li@mpie.de; y.gong@mpie.de; b.gault@mpie.de

T. Colnaghi, A. Marek, M. Rampp
Max Planck Computing and Data Facility
Gießenbachstraße 2, 85748 Garching, Germany

Y. Gong
Department of Materials
University of Oxford
Parks Road, Oxford OX1 3PH, UK

H. Zhang, Y. Yu, M. Wuttig
Institute of Physics (IA)
RWTH Aachen University
52056 Aachen, Germany

The ORCID identification number(s) for the author(s) of this article can be found under https://doi.org/10.1002/adma.202407564

DOI: 10.1002/adma.202407564

Y. Wei
Ecole Polytechnique Fédérale de Lausanne
School of Engineering
Rte Cantonale, Lausanne 1015, Switzerland

B. Gan
Suzhou Laboratory
No.388, Ruoshui Street, SIP, Jiangsu 215123, China

M. Song, Z. Wang
State Key Laboratory of Powder Metallurgy
Central South University
Changsha 410083, China
E-mail: z.wang@csu.edu.cn

Z. Pei
New York University
New York, NY 10012, USA

F. Körmann
Materials Informatics
BAM Federal Institute for Materials Research and Testing
Richard-Willstätter-Str. 11, 12489 Berlin, Germany

B. Gault
Department of Materials
Imperial College
South Kensington, London SW7 2AZ, UK

electron microscopy (TEM)-based approaches are most prevalently used to resolve CSRO,[2b,3b,d,g,5] but reports on the presence and configuration of CSRO have been thus far contradictory, even for samples synthesized in the same conditions (Table S1; Supplementary Text, Supporting Information). Due to the intrinsic limit of two-dimensional projection imaging, it has been pointed out that the observed electron reflections may originate from factors other than CSROs, e.g., planar defects and higher-order Laue zones.[5,6] An alternative, reliable, 3D analytic perspective of CSRO is hence needed to reconcile these controversies, but also to facilitate the use of CSRO in the materials design.

Atom probe tomography (APT) has long been expected to probe CSRO in 3D, but recognizing CSRO has been hindered by its anisotropic spatial resolution and imperfect detection efficiency.[7] Overcoming these limitations by manual analysis has proven impossible.[8] Inspired by other machine learning (ML) methods developed to process complex microscopy and microanalysis data,[9] and building on our previous efforts,[7c,10] we introduce a bottom-up approach to quantify in 3D the CSRO domains in APT data from CoCrNi, termed ML-APT, that does not require any prior knowledge of the CSRO configurations, in contrast with previous work[10] (Supporting Information). The overall flowchart is presented in Figure S1 (Supporting Information). ML-APT enables the identification of CSROs as well as the quantification of the number density of ordered domains, their configurations, elemental site occupancy, and size/morphology. Monte-Carlo simulations are then used to rationalize our analyses, facilitating an understanding of ordering reactions. We finally showcase how to establish a direct processing-CSRO-property relationship, paving the way for further material design opportunities.

2. Results and Discussion

2.1. APT Results

An equiatomic CoCrNi alloy was analyzed in two states, first following the homogenization, and, second, after the homogenization and annealing (Methods and Table S2, Supporting Information). We performed correlative scanning electron microscopy-electron backscattered diffraction (EBSD)-focused ion beam (FIB)-APT to characterize their microstructure in grains of selected orientation (**Figure 1a**), i.e., {002} and {111}. Figure 1b–e details a typical APT analysis from the annealed sample. Figure 1b is a detector hit map with a pattern corresponding to the symmetries of {002} crystallographic planes, and Figure 1c is the 3D atom map reconstructed around this pole. A close-up in Figure 1d shows resolved {002} atomic planes. The reconstruction was calibrated to the reported interplanar spacing of face-centred-cubic (fcc) CoCrNi.[11] Spatial distribution maps[12] are calculated along the depth (z-SDMs) to exploit these most highly resolved signals and to evaluate the CSRO. The z-SDM indicates the characteristic period of each elemental pair along a specific direction, which is similar to a split pair correlation function used in, e.g., TEM.[3c] The z-SDMs of different elemental pairs obtained in a 2-nm voxel are plotted in Figure 1e. The peak-to-peak distance for each elemental pair is the same, suggesting a homogenous solid solution. Typical clustering algorithms in the APT community[8c,13] have been tested but cannot identify CSROs (Figure 1f,g and Supporting Information). A similar analysis along {111} planes is provided in Figure S2 (Supporting Information). The spatial resolution for {022} planes is insufficient to perform subsequent analyses.

2.2. ML-APT Framework

As detailed in **Figure 2a** for $L1_2$-CSRO, for the random solid solution of fcc-based CoCrNi alloys, the elemental occupation of each site is equiprobable. CSRO occurs when particular sites have a higher probability to be occupied by a specific element, e.g. the face-centered sites are more likely to be Cr/Ni while the edges are Co atoms. At higher probability, up to close to 100%, CSRO is established and can facilitate the nucleation of long-range chemical order. The corresponding Co-Co z-SDMs along the <002> from simulated APT data are shown in Figure 2b, and the peaks close to ±0.18 nm and ±0.54 nm are disappearing with the evolution of CSRO. Any type of CSRO can be detected, provided that its signature in the z-SDMs along a particular orientation is clear. This allows us to recognize different CSRO configurations without any prior knowledge, which is conceptually unlike the previous up-bottom strategy with prior possible ordered or CSRO structures.[7c,10]

The ML-APT workflow to reveal CSRO in H/MEA is as follows. First, we generated artificial APT data along <002> or <111> containing either a randomly distributed fcc-matrix or CSRO (Methods). The weak CSRO was not simulated, as the signal to background ratio of the peaks at ΔZ values such as ±0.18 nm and ±0.54 nm is typically too low to confidently identify them experimentally. The FCC and strong CSRO, were labeled as 0 and 1, respectively. Over 10 000 of corresponding z-SDMs patterns are recorded for each orientation (Table S3, Supporting Information). This synthetic data is fed into an optimized 1D convolutional neural network (CNN) to obtain an fcc-matrix/CSRO binary classification model (Figure 2c; Methods and Figure S3a, Supporting Information). Note that a random forest algorithm has been tested but its performance is not better than the applied 1DCNN.[10] ML-APT shows excellent performance for both simulated and experimental test datasets (Methods and Figures S3b–d and S4, Supporting Information). It is further tested on a set of physically-informed large-scale CoCrNi artificial APT data with $L1_2$-CSRO domains with a diameter of 0.7–2.0 nm (Methods, Supporting Information), and ML-APT distinguishes these well (Figure S5 and Supporting Information). The gradient-weighted class activation mapping,[7c,14] which uses gradients of any target concept flowing into the final convolutional layer to produce a coarse localization map highlighting the important regions in the image for predicting the concept, reveals that ML-APT performs the classification by focusing on the specific peaks of the z-SDMs that can be used to accurately classify the fcc/CSRO in both simulated and experimental data (Figure S6, Supporting Information). Finally, experimental z-SDMs were subjected to preprocessing and then input into ML-APT to obtain 3D CSRO distributions (Figure 2d; Methods, Supporting Information).

2.3. 3D Perspective of CSRO

Typical examples of 3D distributions of CSRO domains obtained from ML-APT, applied to Co–Co, Cr–Cr, and Ni–Ni, are presented

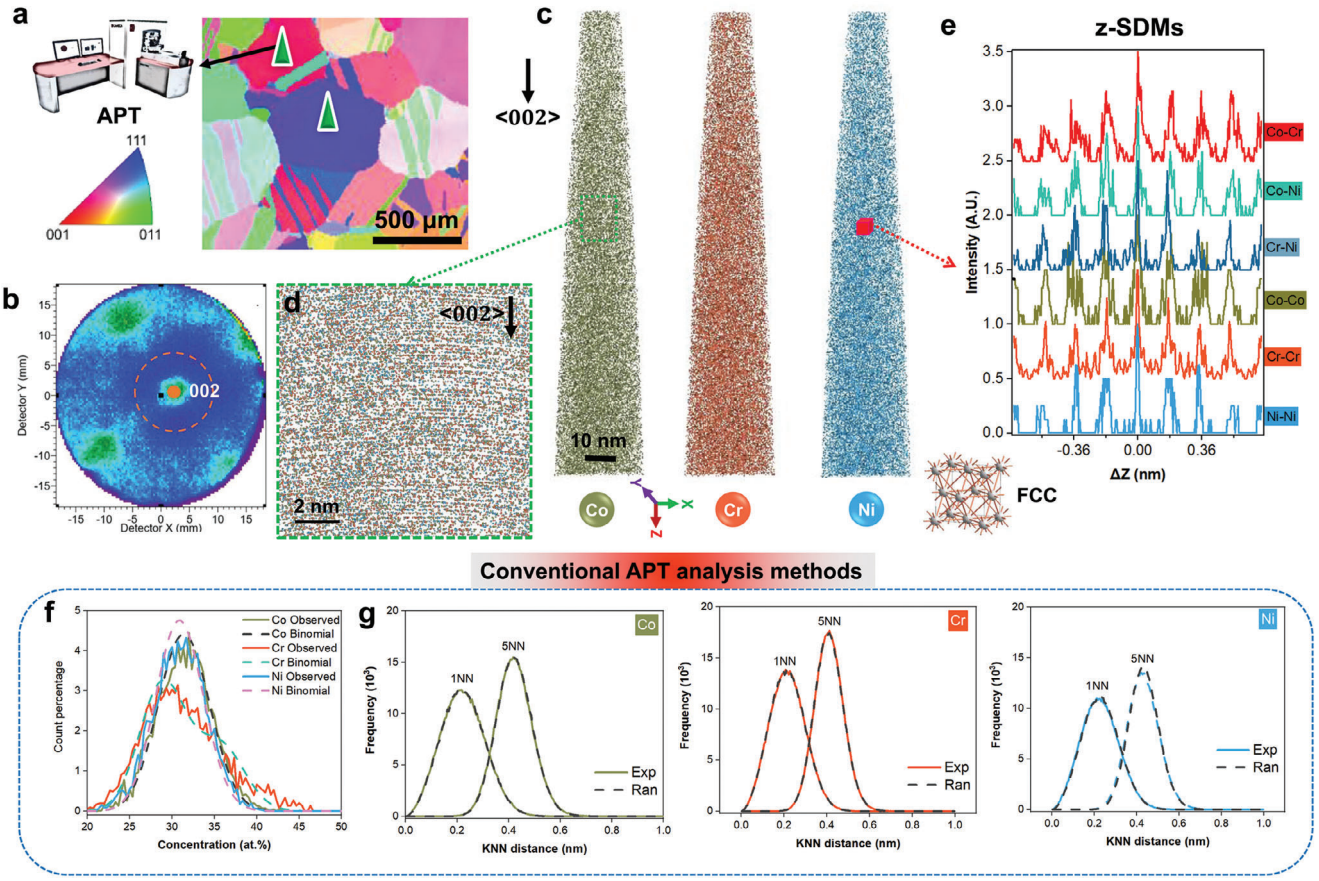

Figure 1. Typical APT data of the equiatomic CoCrNi alloy after annealing at 1273K for 120 h and conventional data analysis to look for CSRO. a) The EBSD inverse pole figure highlights the grains used for APT experiments. b) Representative 2D detector hit map. One centric {002} crystallographic pole is labeled. c) Precise 3D APT reconstruction along the <002> orientation. d) Local close-up of a thin slice in (c) along the <002>. e) z-SDMs of different elemental pairs in a representative 2-nm voxel in (c). Its signature corresponds to the fcc structure and its unit cell is given. Two kinds of conventional APT analysis approaches: f) frequency distribution analysis of Co, Cr, and Ni atoms compared to the binomial random distributions, and g) *k*-nearest neighbor (KNN) distance analysis (k = 1 and 5) of Co-Co, Cr-Cr, and Ni-Ni elemental pairs. Exp and Ran labels correspond to the results obtained by experimental and random-labeled datasets, respectively.

in **Figures** 3 and S7 (Supporting Information) along <002> and <111>, respectively. Cross-species elemental pairs were not analyzed to avoid possible biases arising from differences in evaporation fields affecting the spatial resolution[15] and this same-species information is enough to analyze the CSRO (Supporting Information). Figure 3a shows a typical spatial distribution of these domains with a near-spherical morphology (Figure S8, Supporting Information). Its z-SDM and that of the remaining fcc matrix data are plotted in Figure S9 (Supporting Information), matching well with those from simulations as outlined in Figure 2b. Figure 3b–d shows size distributions of domains in which the Co–Co, Cr–Cr, and Ni–Ni are classified as ordered, respectively. The Pearson's correlation coefficient (PCC) and contingency coefficient (μ)[16] are used to test the statistical significance of the difference between these distributions and a chemically randomized dataset, with μ found more sensitive than PCC to characterize such subtle differences. We defined a threshold to classify the (non-)randomness at 0.25. The choice of 0.25 is explained in Methods (Supporting Information). The Ni-Ni distribution is non-random, with a μ of 0.32, especially when the domain has more than 35 atoms (<1 nm) (Figure 3e), while the distribution of the two other elements is closer to random (μ<0.25). Figure 3d,e demonstrates that these CSRO domains with sizes below 35 atoms are primarily statistically and randomly formed. Considering the average diameter of one CSRO is generally ≈1 nm, it is reasonable to conclude that domains with fewer than 35 atoms are mostly disordered. Figure 3f is an example of the Ni–Ni CSRO domain, and the corresponding Ni–Ni z-SDM is plotted in Figure 3g, showcasing an interplanar spacing of Ni atoms is twice as large as that in the fcc-matrix (Figure 1e) (those of Cr–Cr and Ni–Ni still keep 0.18 nm as shown in Figure S10, Supporting Information), which matches the $L1_2/DO_{22}$-type structure with the Ni–Ni repulsion on {100} as explained in **Figure** 4a. Although other crystal structures may also match this repulsion scenario, we use the most often experimentally observed $L1_2/DO_{22}$-type structures.[5b] For comparisons, along the <111>, the three kinds of CSROs are all different from the random state with μ ≥ 0.25 (Figure S7b–d, Supporting Information). This suggests that there is either Co/Cr/Ni repulsion on {111}, which matches the $L1_1$-type structure, as detailed in Figure S7e (Supporting Information) and Figure 4b.

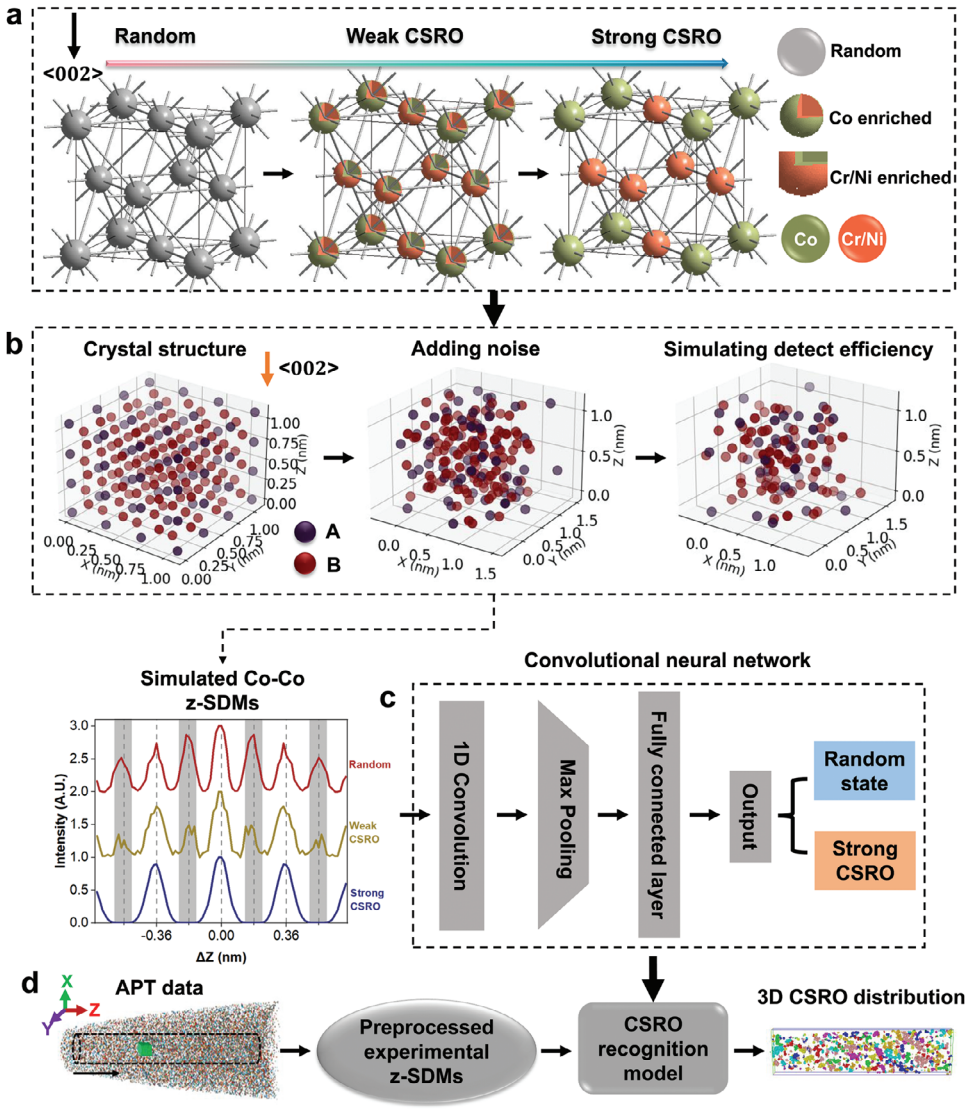

Figure 2. Proposed ML-APT framework to recognize multi-type CSROs in CoCrNi alloys. a) Unit cells of random-fcc, weak, and strong $L1_2$-CSRO. b) Typical Co-Co z-SDMs along the <002> with the evolution of CSRO after performing APT simulation. c) Schematic diagram of the optimised 1D CNN structure to obtain a random-fcc/CSRO recognition model. d) Flowchart of processing experimental data to obtain 3D CSRO distribution.

Figure 4c,d provides values of μ for the two studied material states and orientations. Along {002} planes, the value of μ of Co–Co or Cr–Cr CSROs remains below 0.25. Non-statistical Ni–Ni CSRO rises from 0.18 to 0.27 after annealing at 1273K for 120 h, with a number density of 4.81×10^{25} m^{-3} of CSRO domains with atomic configurations matching the $L1_2/DO_{22}$ structures with the Ni-Ni repulsion on {100} (Figure 4a,e). Note that the probability for the $L1_0$ structure is much lower compared to that for the $L1_2/DO_{22}$ considering only one elemental pair has an obvious repulsive tendency. Along {111} planes, after the homogenization, values of μ for Co–Co and Ni-Ni CSRO are close to or above 0.25, suggesting the existence of $L1_1$-domains with the Co/Ni repulsion on the {111}, with a number density in the range of $2.98–3.18 \times 10^{25}$ m^{-3} (Figure 4b,e). After the annealing, the values of μ of Co–Co, Cr–Cr, and Ni–Ni pairs are above 0.25, matching with the $L1_1$-type structure with Co–Co/Cr–Cr/Ni–Ni repulsions on the {111}, with a number density of 4.73×10^{25} m^{-3}, 4.66×10^{25} m^{-3}, and 4.73×10^{25} m^{-3}, as determined from Co–Co, Cr–Cr, and Ni–Ni pairs, respectively (Figure 4b,e). Only $L1_1$-domains exist after the homogenization, and their number density increases after the annealing, during which a high density of $L1_2/DO_{22}$-domains appears (Figure 4e,f). Overall, the number density of CSRO domains is approximately three times after the annealing compared to that after the homogenization. It should be pointed out that {111} plane has four rotational variants, i.e., {111} (i.e., $(\bar{1}11)$, (111), $(1\bar{1}1)$, or $(11\bar{1})$), and Figure 4e is the analysis of the given population of CSRO-domains along only one variant that can be imaged in that particular APT dataset with sufficient resolution to perform the analysis. An additional dataset obtained along another {111} variant leads to comparable results (Figure S20 and Supporting Information). One can estimate the overall number densities by extrapolating the obtained number

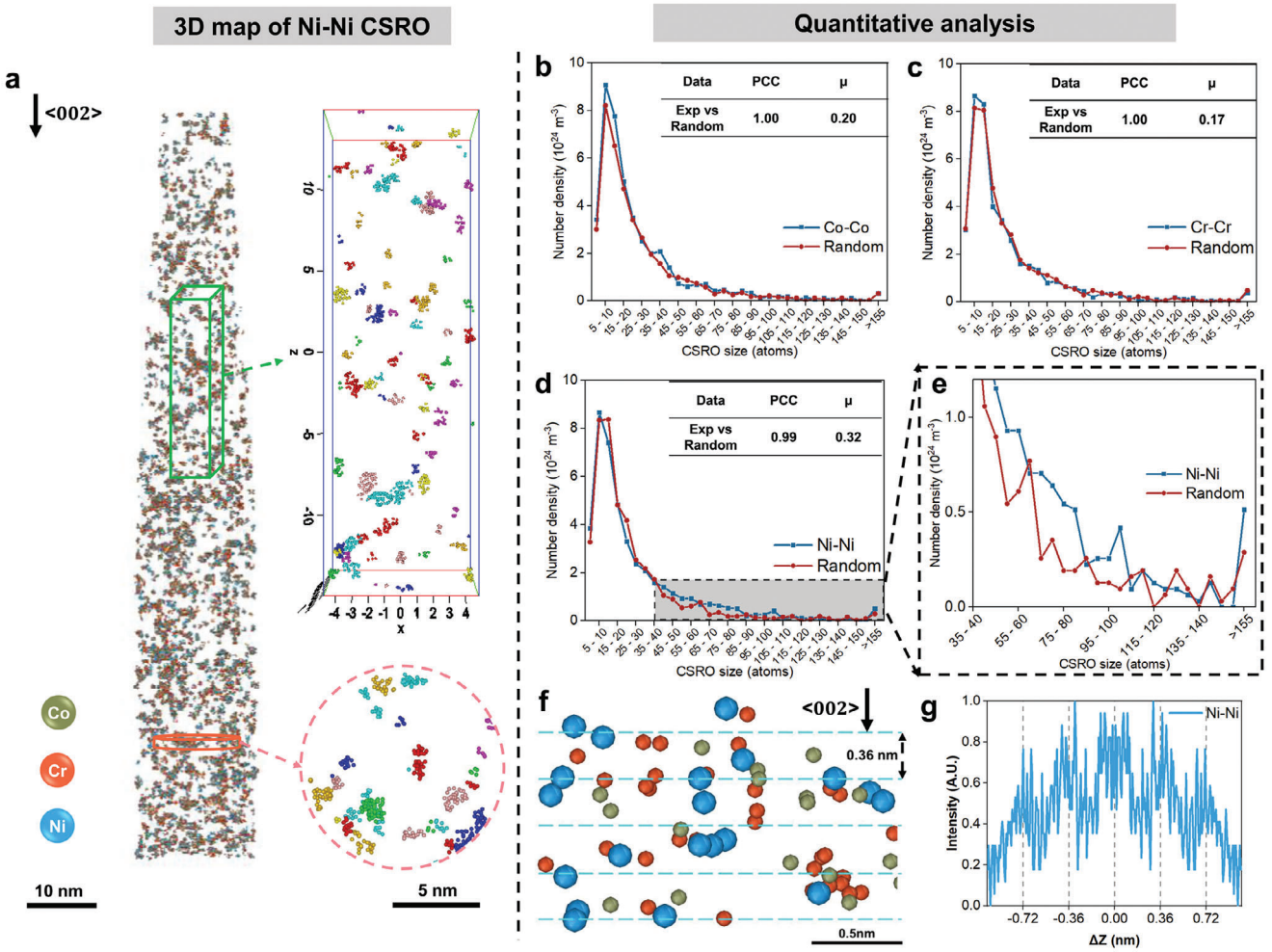

Figure 3. 3D quantitative analysis of CSRO along <002> in the annealed CoCrNi alloy. a) 3D distribution of Ni-Ni CSROs with the mapping of elements. The front and top views of typical clusters are provided. Different colors mark different CSRO domains. b–d) Size distributions of the identified Co–Co, Cr–Cr, and Ni–Ni CSROs, respectively. The results from the chemically randomized dataset (Methods, Supporting Information) are compared with Pearson's correlation coefficient (PCC) and Pearson contingency coefficient (μ). This CSRO size refers to the APT-counted atoms and the size of 55 atoms ideally corresponds to a 1-nm cube. An upper tail occurring at 155 atoms appears, because we have added all those containing over 155 atoms into this particular bin. e) Local enlargement of the colored region in (d) which is different from the random curve. f) 3D atom map of a typical Ni-Ni CSRO domain extracted from (e). g) Its corresponding Ni-Ni z-SDM (Cr–Cr and Co–Co z-SDMs are provided in Figure S10, Supporting Information).

density on one {111} plane and multiplying it by four, enabling a more accurate quantitative relationship between CSRO and associated properties. For example, there are more than 36 additional CSRO domains within a 10^3-nm^3 volume after the annealing as compared to that after the homogenization, which will influence materials' properties, including for instance the electrical resistivity as discussed below. During the entire process, the CSROs almost keep the spherical shape (Figure S8, Supporting Information) with the size of 20–155 APT-counted atoms (0.7–1.5 nm in diameter) (Figure 3 and Figure S7, Supporting Information). Note that these observed domains along {002} and {111} are not the same ones. A comparison of the compositions between CSRO domains and raw data suggests that there is no obvious statistical difference between them, indicating that only the ordering changed and not the composition (A quantitative explanation is provided in Supporting Information). Moreover, we compared the results from laser and voltage pulsing modes (Supporting Information), as shown in Figure S11 (Supporting Information), which show comparable results, which can be rationalized based on previous reports of the moderate changes in the depth resolution between voltage and laser pulsing modes.[17] Analysis of the combined elemental pairs for each individual domain is not recommended due to the nature of the CSRO, which reflects the local elemental fluctuation at a very early stage of thermally activated ordering.

2.4. Electrical Response

The occurrence of CSRO in solid solutions is often associated with the modifications of physical properties.[8a,b,18] The influence of CSRO on the mechanical properties of CoCrNi has been studied widely,[2b,3d,5a,11a] with inconsistent conclusions, but functional properties have only rarely been investigated. Here,

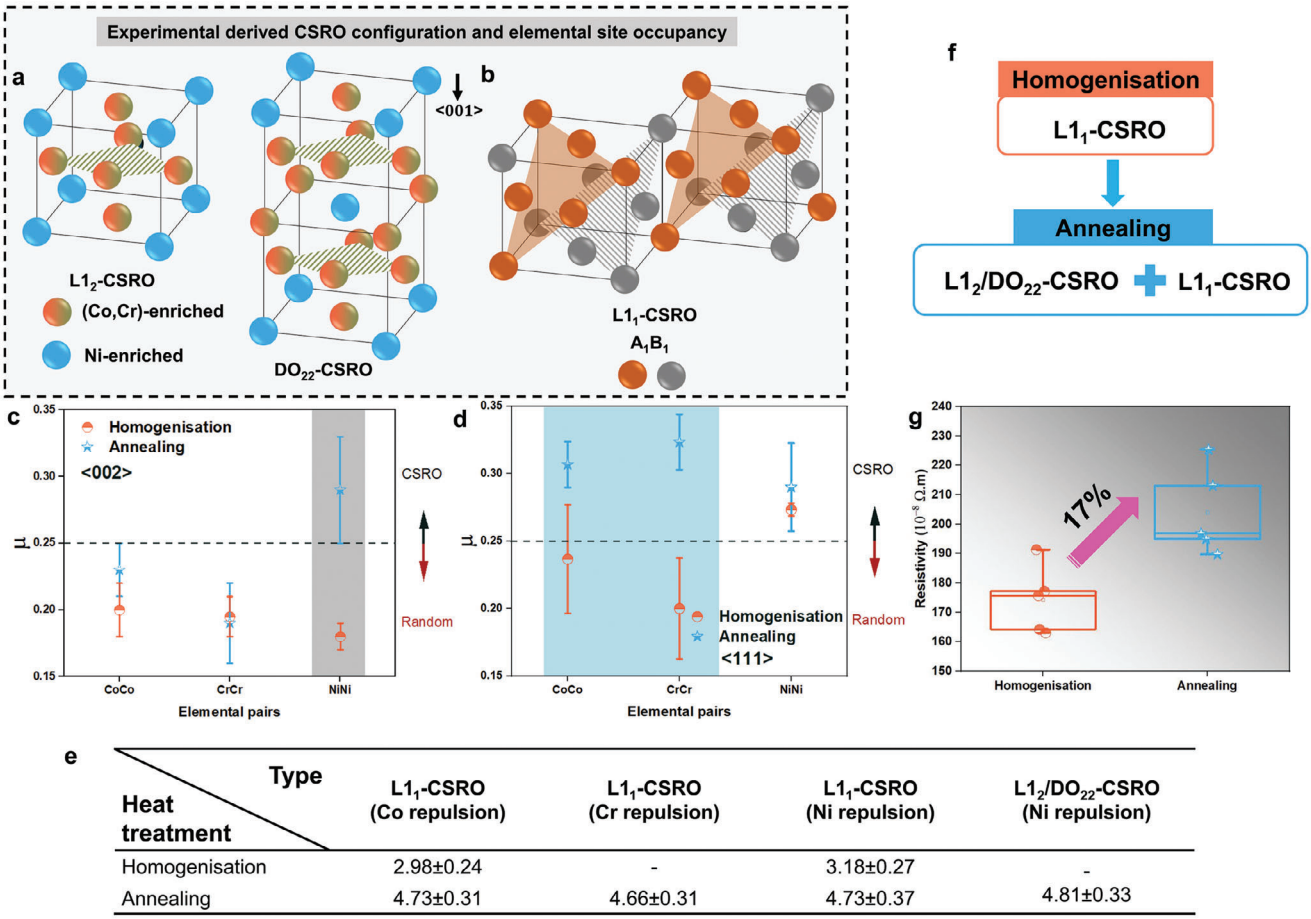

e

Heat treatment \ Type	L1$_1$-CSRO (Co repulsion)	L1$_1$-CSRO (Cr repulsion)	L1$_1$-CSRO (Ni repulsion)	L1$_2$/DO$_{22}$-CSRO (Ni repulsion)
Homogenisation	2.98±0.24	-	3.18±0.27	-
Annealing	4.73±0.31	4.66±0.31	4.73±0.37	4.81±0.33

Figure 4. 3D atomic-level details of multi-type CSROs in CoCrNi alloys under different heat treatments and arising electrical resistivity change. a) The L1$_2$/DO$_{22}$-CSRO structure with the Ni–Ni repulsion on {100}. b) The L1$_1$-CSRO structure with the A-A or B-B repulsion on {111}. Element A or B refers to sites that are enriched in Co, Cr, or Ni but cannot be the same simultaneously (an intuitive explanation is given in Figure S7e, Supporting Information). c,d) Changes of Pearson contingency coefficient (μ) under different heat treatments along <002> and <111>, respectively. The colored regions highlight the changes of μ after the annealing. Three APT datasets were analyzed to obtain the statistical results for each data point. A value of μ = 0.25 is regarded as the threshold between CSRO and random states. e) Number-density change (×10^{25} m^{-3}) of different types of CSROs under heat treatment. f) Derived CSRO structural evolution from homogenization to annealing. The corresponding CSRO configurations are plotted in (a) and (b). g) Evolutions of electrical resistivity under different heat treatments.

we measured the electrical resistivity of the two material states (Methods). The annealing-induced multiple CSROs in CoCrNi alloys resulted in a 17% rise in the room-temperature electrical resistivity (Figure 4g), higher than previous reports (+4.8%) in ref.[5a] which can be explained by the formation of a higher density of CSRO domains during the furnace cooling compared to a quench. This reveals a high sensitivity of the electrical resistivity upon changes in the CSRO state, maybe more so than the mechanical response. This remarkable increase in resistivity implies that the increasing CSRO might lead to a reduced electronic density of states at the Fermi level, consistent with the previous density functional theory calculations in the CoCrNi system.[19]

2.5. Monte-Carlo Simulation

ML accelerated ab initio Monte-Carlo (MC) simulations (Methods, Supporting Information) were performed to predict the temperature-dependent equilibrium CSROs and associated crystalline structures.[20] Calculated temperature-dependent heat capacities reveal two peaks due to first-order phase transformations (Figure S12, Supporting Information). One occurs at around 900K, which is confirmed by differential scanning calorimetry (DSC), and the second occurs at around 225K which is below the detection limit of DSC due to sluggish diffusion kinetics at low temperatures. Predicted first NN Warren-Cowley parameters (Methods) suggested repulsion of Cr–Cr, Co–Ni, Co–Co and attractions of Ni–Ni, Cr–Ni, Co–Cr above the phase transformation peak, as shown in Figure S13 (Supporting Information). To identify the possibly locally appearing crystalline ordered clusters in the CSROs regime, **Figure** 5a,b visualize the calculated CSRO diffuse intensity map (α_q) (Methods, Supporting Information) in the (001) and (111) planes, respectively, at 1000K. For the (001), a (1, 0.5, 0) special point is revealed for Cr–Cr, suggesting, e.g., a DO$_{22}$ ordering.[21] Besides, a (001) peak is also presented for the Ni–Ni and Co–Co pairs: local clusters of L1$_2$ or L1$_0$ ordering are

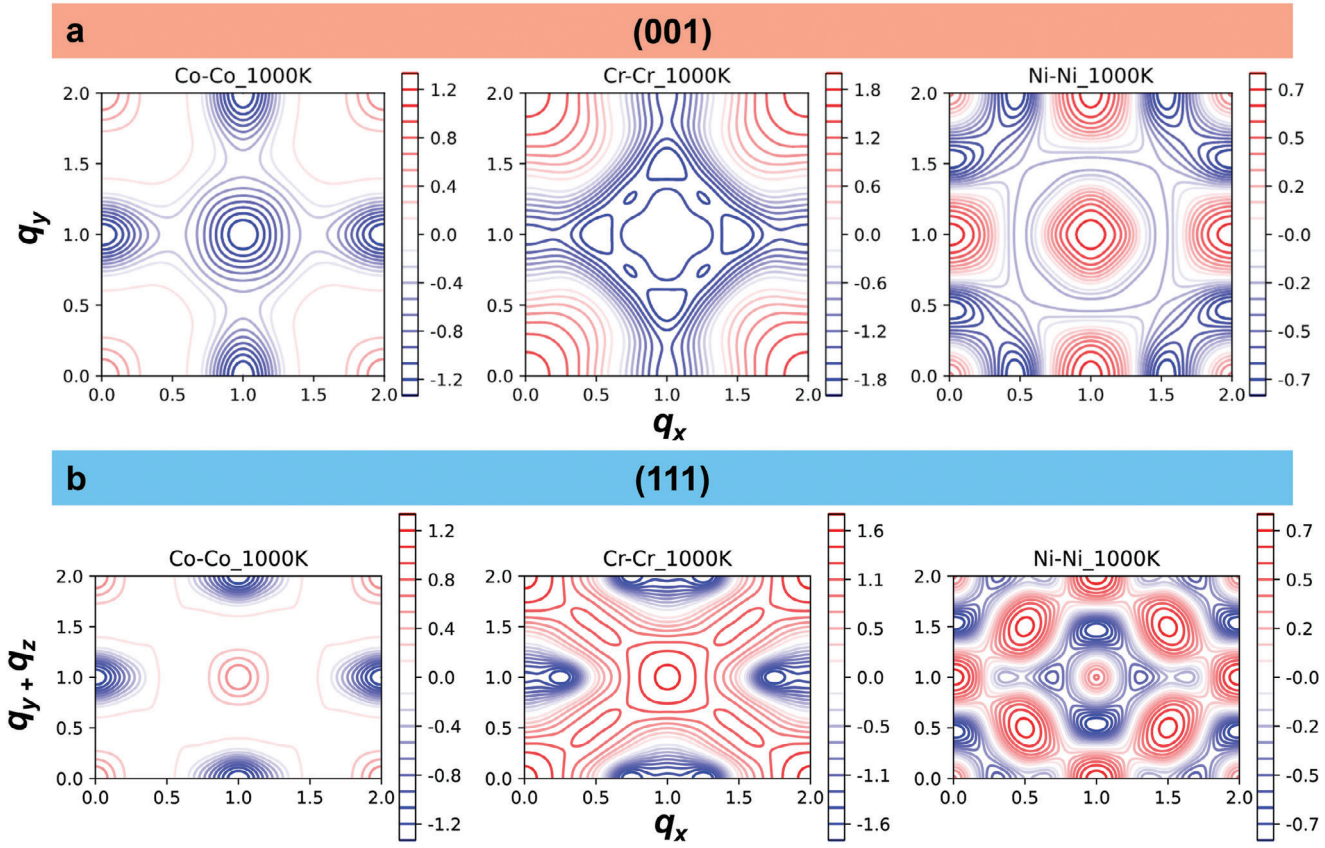

Figure 5. CSROs predicted by Monte-Carlo simulations. a,b) Predicted CSRO diffuse intensity map, α_q, of Co–Co, Cr–Cr, and Ni–Ni pairs at 1000K in (001) and (111) planes, respectively. The reciprocal space vectors are given in units of $2\pi/a$, where a is the lattice parameter.

suggested for these two. The intensity of $L1_2$ or $L1_0$ consistent CSRO peak is strongly enhanced by magnetic effects (Supporting Information). Further peak analysis in the 3D reciprocal space found (0.5, 0.5, 0.5) maxima for Cr–Cr and Ni–Ni pairs, which are also revealed by projecting the calculated α_q in the (111) as shown in Figure 5b, which would be consistent with local $L1_1$ configurations (i.e., ordering along <111>). Compared with APT measurements (Figure 4), ordering along <002> for Ni–Ni, as well as ordering along <111> for Cr–Cr and Ni–Ni are confirmed by MC simulations. For Co–Co pairs, the correlations related to $L1_1$ are less pronounced (Figure S17, Supporting Information). Previous studies predominantly suggested the presence of $L1_1$ and/or $L1_2$- CSRO with Cr-Cr repulsion. Here, we conducted further investigations by studying an additional CoCrNi sample that was annealed at 1273K for 120 h followed by quenching, allowing for comparison with previous furnace cooling condition to address this discrepancy (Supporting Information).

Although the ML-APT enables tomographic imaging of CSRO in CoCrNi alloys, there are some inherent limitations at the current status, as for all experimental techniques. First, high-quality APT experimental data is needed (see Supporting Information for how to determine the quality), to maximize the spatial resolutions, to enable more accurate recognition of CSRO patterns. Enhancing data quality, and maybe even breaking the limitation for analysis of only specific sets of planes, could arise from better modeling atom probe tomography[22] to optimize data acquisition parameters and enable the analysis of the cross-species elemental pairs, even if the compositional complexity of the material will impose limits in the achievable precision.[7b] Moreover, voxelization (here $1 \times 1 \times 1$ nm^3) lowers the accuracy and may preclude the identification of small CSRO domains. With higher data quality, the ML-APT could be used with smaller voxels. Finally, there could be ways to directly apply other 3D-based ML techniques to detect CSRO after enhancing the APT data quality.[23]

3. Conclusion

To conclude, the proposed ML-APT approach enables us to settle previous debates on CSRO in CoCrNi alloys, and evidence atomic-scale details of CSRO beyond the state-of-the-art. It simultaneously resolves CSRO at both the individual-domain and overall (statistical) levels. In comparison to other approaches for CSRO characterization, our proposed ML-APT analysis only relies on the measured APT mass spectra and is hence independent of interatomic potentials needed to interpret CSRO from X-ray/neutron techniques.[4] Moreover, ML-APT provides 3D elemental-specific information and is hence capable of identifying multiple types of CSRO (Figures 3 and 4). The observed CSRO configurations were rationalized herein by Monte-Carlo simulations. The electrical response could be a better indicator of CSROs than mechanical properties. The individual influence

of CSRO on the mechanical properties is seemly limited at room temperature, whereas, the co-existing CSRO and medium-range order could be a better approach to designing new H/MEAs with better (cryogenic) mechanical properties via adjusting the processing parameters (e.g., thermal history[24] and deformation)[25] or microalloying (e.g., adding Ti or Al).[26] Our method can be generally used for other H/MEAs as well as for complex engineering materials.

Supporting Information

Supporting Information is available from the Wiley Online Library or from the author.

Acknowledgements

This work was primarily supported by the research fellowship provided by the Alexander von Humboldt Foundation and the Max Planck research network on big-data-driven materials science (BiGmax). BG acknowledges financial support from the ERC via the funding of the project SHINE 771602. Y.G., S.G., and F.K. acknowledge the LRP and MC/Python simulation packages by Alexander Shapeev and funding from Deutsche Forschungsgemeinschaft (within the SPP 2006 and DFG 5080/3-1). Y.G. acknowledges the Next Generation TATARA Project sponsored by the Cabinet of Japan. ZW acknowledges the Natural Science Foundation of Hunan Province (Grant No. 2022JJ30712) and the support from State Key Laboratory of Powder Metallurgy, Central South University, Changsha, China. Frank Stein and Andreas Jansen are acknowledged for their help with DSC measurements. Uwe Tezins and Andreas Sturm are acknowledged for their support of the FIB and APT facilities. Alisson Kwiatkowski da Silva and Shaolou Wei are acknowledged for fruitful discussions.

Open access funding enabled and organized by Projekt DEAL.

Conflict of Interest

The authors declare no conflict of interest.

Author Contributions

Y.L., Y.G., Z.W., and B.G. designed the project. Y.L. is the lead experimental/data scientist. M.S. and B.i.G. prepared the materials and heat treatments. Y.L. performed the FIB/APT experiments and analyzed the APT data with the help of B.G. Y.L. programmed the machine learning framework with the help of Y.W. and T.C. H.Z. and Y.Y. performed the electrical resistivity measurements. Y.G. programmed and performed the MC simulations. Y.G. and S.G. performed the ab initio calculations and constructed the ML potentials. Y.L., Y.G., Z.W., and B.G. wrote the manuscript. All authors contributed to the discussion of the results and commented on the manuscript.

Data Availability Statement

The data that support the findings of this study are openly available in figshare at https://doi.org/10.6084/m9.figshare.24274780, reference number 1. The ML-APT software is available at the GitHub address https://github.com/a356617605.

Keywords

artificial intelligence, atomic-scale characterization, high/medium-entropy alloys, local chemical ordering, tomographic imaging

Received: May 28, 2024
Revised: July 24, 2024
Published online: August 12, 2024

[1] a) W. Sun, Y. Zhu, R. Marceau, L. Wang, Q. Zhang, X. Gao, C. Hutchinson, *Science* **2019**, *363*, 972; b) Y. Li, B. Holmedal, H. Li, L. Zhuang, J. Zhang, Q. Du, *Materialia* **2018**, *4*, 431; c) J. Zhang, D. Zhou, X. Pang, B. Zhang, Y. Li, B. Sun, R. Z. Valiev, D. Zhang, *Acta Mater.* **2022**, *244*, 118540; d) R. Zhang, S. Zhao, C. Ophus, Y. Deng, S. J. Vachhani, B. Ozdol, R. Traylor, K. C. Bustillo, J. W. Morris, D. C. Chrzan, M. Asta, A. M. Minor, *Sci. Adv.* **2019**, *5*, eaax2799; e) G. Wu, S. Balachandran, B. Gault, W. Xia, C. Liu, Z. Rao, Y. Wei, S. Liu, J. Lu, M. Herbig, W. Lu, G. Dehm, Z. Li, D. Raabe, *Adv. Mater.* **2020**, *32*, 2002619.

[2] a) E. P. George, D. Raabe, R. O. Ritchie, *Nat. Rev. Mater.* **2019**, *4*, 515; b) R. Zhang, S. Zhao, J. Ding, Y. Chong, T. Jia, C. Ophus, M. Asta, R. O. Ritchie, A. M. Minor, *Nature* **2020**, *581*, 283; c) C. Niu, C. R. LaRosa, J. Miao, M. J. Mills, M. Ghazisaeidi, *Nat. Commun.* **2018**, *9*, 1363; d) F. Zhang, Y. Wu, H. Lou, Z. Zeng, V. B. Prakapenka, E. Greenberg, Y. Ren, J. Yan, J. S. Okasinski, X. Liu, Y. Liu, Q. Zeng, Z. Lu, *Nat. Commun.* **2017**, *8*, 15687; e) S. Zhao, G. M. Stocks, Y. Zhang, *Acta Mater.* **2017**, *134*, 334.

[3] a) X. Chen, Q. Wang, Z. Cheng, M. Zhu, H. Zhou, P. Jiang, L. Zhou, Q. Xue, F. Yuan, J. Zhu, X. Wu, E. Ma, *Nature* **2021**, *592*, 712; b) L. Zhou, Q. Wang, J. Wang, X. Chen, P. Jiang, H. Zhou, F. Yuan, X. Wu, Z. Cheng, E. Ma, *Acta Mater.* **2022**, *224*, 117490; c) Q. Ding, Y. Zhang, X. Chen, X. Fu, D. Chen, S. Chen, L. Gu, F. Wei, H. Bei, Y. Gao, M. Wen, J. Li, Z. Zhang, T. Zhu, R. O. Ritchie, Q. Yu, *Nature* **2019**, *574*, 223; d) M. Zhang, Q. Yu, C. Frey, F. Walsh, M. I. Payne, P. Kumar, D. Liu, T. M. Pollock, M. D. Asta, R. O. Ritchie, A. M. Minor, *Acta Mater.* **2022**, *241*, 118380; e) J.-P. Du, P. Yu, S. Shinzato, F. Meng, Y. Sato, Y. Li, Y. Fan, S. Ogata, *Acta Mater.* **2022**, *240*, 118314; f) F. Walsh, M. Asta, R. O. Ritchie, *Proc. Natl. Acad. Sci. U.S.A.* **2021**, *118*, 2020540118; g) H. Hsiao, R. Feng, H. Ni, K. An, J. Poplawsky, P. Liaw, J. Zuo, *Nat. Commun.* **2022**, *13*, 6651.

[4] a) F. X. Zhang, S. Zhao, K. Jin, H. Xue, G. Velisa, H. Bei, R. Huang, J. Y. P. Ko, D. C. Pagan, J. C. Neuefeind, W. J. Weber, Y. Zhang, *Phys. Rev. Lett.* **2017**, *118*, 205501; b) K. Inoue, S. Yoshida, N. Tsuji, *Phys. Rev. Mater.* **2021**, *5*, 085007.

[5] a) L. Li, Z. Chen, S. Kuroiwa, M. Ito, K. Yuge, K. Kishida, H. Tanimoto, Y. Yu, H. Inui, E. P. George, *Acta Mater.* **2023**, *243*, 118537; b) F. Walsh, M. Zhang, R. O. Ritchie, A. M. Minor, M. Asta, *Nat. Mater.* **2023**, *22*, 926.

[6] F. G. Coury, C. Miller, R. Field, M. Kaufman, *Nature* **2023**, *622*, 742.

[7] a) B. Gault, A. Chiaramonti, O. Cojocaru-Mirédin, P. Stender, R. Dubosq, C. Freysoldt, S. K. Makineni, T. Li, M. Moody, J. M. Cairney, *Nat. Rev. Methods Primers* **2021**, *1*, 51; b) B. Gault, B. Klaes, F. F. Morgado, C. Freysoldt, Y. Li, F. De Geuser, L. T. Stephenson, F. Vurpillot, *Microsc. Microanal.* **2022**, *28*, 1116; c) Y. Li, X. Zhou, T. Colnaghi, Y. Wei, A. Marek, H. Li, S. Bauer, M. Rampp, L. T. Stephenson, *NPJ Comput Mater* **2021**, *7*, 8.

[8] a) R. K. W. Marceau, A. V. Ceguerra, A. J. Breen, M. Palm, F. Stein, S. P. Ringer, D. Raabe, *Intermetallics* **2015**, *64*, 23; b) R. K. W. Marceau, A. V. Ceguerra, A. J. Breen, D. Raabe, S. P. Ringer, *Ultramicroscopy* **2015**, *157*, 12; c) R. Hu, S. Jin, G. Sha, *Prog. Mater Sci.* **2022**, *123*, 100854.

[9] a) F. Oviedo, Z. Ren, S. Sun, C. Settens, Z. Liu, N. T. P. Hartono, S. Ramasamy, B. L. DeCost, S. I. P. Tian, G. Romano, A. Gilad Kusne, T. Buonassisi, *NPJ Comput Mater* **2019**, *5*, 60; b) J. A. Aguiar, M. L. Gong, R. R. Unocic, T. Tasdizen, B. D. Miller, *Sci. Adv.* **2019**, *5*, eaaw1949; c) Y.-F. Shen, R. Pokharel, T. J. Nizolek, A. Kumar, T. Lookman, *Acta Mater.* **2019**, *170*, 118.

[10] Y. Li, Y. Wei, Z. Wang, X. Liu, T. Colnaghi, L. Han, Z. Rao, X. Zhou, L. Huber, R. Dsouza, Y. Gong, J. Neugebauer, A. Marek, M. Rampp, S. Bauer, H. Li, I. Baker, L. T. Stephenson, B. Gault, *Nat. Commun.* **2023**, *14*, 7410.

[11] a) B. Yin, S. Yoshida, N. Tsuji, W. Curtin, *Nat. Commun.* **2020**, *11*, 2507; b) M. P. Agustianingrum, S. Yoshida, N. Tsuji, N. Park, *J. Alloys Compd.* **2019**, *781*, 866.
[12] a) B. P. Geiser, T. F. Kelly, D. J. Larson, J. Schneir, J. P. Roberts, *Microsc. Microanal.* **2007**, *13*, 437; b) M. P. Moody, B. Gault, L. T. Stephenson, D. Haley, S. P. Ringer, *Ultramicroscopy* **2009**, *109*, 815.
[13] a) P. Dumitraschkewitz, S. S. A. Gerstl, L. T. Stephenson, P. J. Uggowitzer, S. Pogatscher, *Adv. Eng. Mater.* **2018**, *20*, 1800255; b) B. Gault, M. P. Moody, J. M. Cairney, S. P. Ringer, *Atom Probe Microscopy*, Springer, Berlin **2012**.
[14] R. R. Selvaraju, M. Cogswell, A. Das, R. Vedantam, D. Parikh, D. Batra, *Proc. IEEE Int. Conf. Comput. Vis.* **2017**, 618.
[15] F. Vurpillot, A. Bostel, E. Cadel, D. Blavette, *Ultramicroscopy* **2000**, *84*, 213.
[16] M. P. Moody, L. T. Stephenson, A. V. Ceguerra, S. P. Ringer, *Microsc. Res. Tech.* **2008**, *71*, 542.
[17] B. Gault, M. Müller, A. La Fontaine, M. P. Moody, A. Shariq, A. Cerezo, S. P. Ringer, G. D. W. Smith, *J. Appl. Phys.* **2010**, 108.
[18] a) H. Thomas, *Z. Phys.* **1951**, *129*, 219; b) Z. Pei, R. Li, M. C. Gao, G. M. Stocks, *NPJ Comput. Mater.* **2020**, *6*, 122.
[19] A. Tamm, A. Aabloo, M. Klintenberg, M. Stocks, A. Caro, *Acta Mater.* **2015**, *99*, 307.
[20] S. Ghosh, V. Sotskov, A. V. Shapeev, J. Neugebauer, F. Körmann, *Phys. Rev. Mater.* **2022**, *6*, 113804.
[21] U. Kulkarni, S. Banerjee, *Acta Metall.* **1988**, *36*, 413.
[22] a) C. Oberdorfer, S. M. Eich, M. Lütkemeyer, G. Schmitz, *Ultramicroscopy* **2015**, *159*, 184; b) F. Vurpillot, C. Oberdorfer, *Ultramicroscopy* **2015**, *159*, 202.
[23] Z. Rao, Y. Li, H. Zhang, T. Colnaghi, A. Marek, M. Rampp, B. Gault, *Scripta Mater.* **2023**, *234*, 115542.
[24] G. Tang, Z. Zhang, Y. Liu, Y. Wang, X. Wu, X. Liu, *Mater. Des.* **2023**, *225*, 111572.
[25] a) M. Heczko, V. Mazánová, C. E. Slone, M. Shih, E. P. George, M. Ghazisaeidi, J. Polák, M. J. Mills, *Scripta Mater.* **2021**, *202*, 113985; b) Y. M. Eggeler, K. V. Vamsi, T. M. Pollock, *Annu. Rev. Mater. Res.* **2021**, *51*, 209.
[26] a) Y. Zhao, T. Yang, Y. Tong, J. Wang, J. Luan, Z. Jiao, D. Chen, Y. Yang, A. Hu, C. Liu, *Acta Mater.* **2017**, *138*, 72; b) N. Yao, T. Lu, K. Feng, B. Sun, R.-Z. Wang, J. Wang, Y. Xie, P. Zhao, B. Han, X.-C. Zhang, S.-T. Tu, *Acta Mater.* **2022**, *236*, 118142.